



Deposited via The University of Sheffield.

White Rose Research Online URL for this paper:

<https://eprints.whiterose.ac.uk/id/eprint/215326/>

Version: Accepted Version

Article:

Evans, H., Andrews, R., Abedi, F.A. et al. (2024) Evidence for peri-lacunar remodeling and altered osteocyte lacuno-canalicular network in mouse models of myeloma-induced bone disease. JBMR Plus, 8 (9). ziae093. ISSN: 2473-4039

<https://doi.org/10.1093/jbmrpl/ziae093>

© 2024 The Authors. Except as otherwise noted, this author-accepted version of a journal article published in JBMR Plus is made available via the University of Sheffield Research Publications and Copyright Policy under the terms of the Creative Commons Attribution 4.0 International License (CC-BY 4.0), which permits unrestricted use, distribution and reproduction in any medium, provided the original work is properly cited. To view a copy of this licence, visit <http://creativecommons.org/licenses/by/4.0/>

Reuse

This article is distributed under the terms of the Creative Commons Attribution (CC BY) licence. This licence allows you to distribute, remix, tweak, and build upon the work, even commercially, as long as you credit the authors for the original work. More information and the full terms of the licence here:

<https://creativecommons.org/licenses/>

Takedown

If you consider content in White Rose Research Online to be in breach of UK law, please notify us by emailing eprints@whiterose.ac.uk including the URL of the record and the reason for the withdrawal request.

1 **Evidence for peri-lacunar remodeling and altered osteocyte lacuno-canalicular network**
2 **in mouse models of myeloma-induced bone disease**

3 Holly Evans^{1*}, Rebecca Andrews^{1,2*}, Fatma Ali Abedi¹, Alexandria Sprules¹, Jacob Trend³,
4 Goran Lovric⁴, Alanna Green¹, Andrew Chantry^{1,2}, Claire Clarkin³, Janet Brown^{1,2} and
5 Michelle Lawson¹

6 *joint first authors

7 **Affiliations**

8 ¹Division of Clinical Medicine and Mellanby Centre for Musculoskeletal Research, School of
9 Medicine and Population Health, Faculty of Health, University of Sheffield, Sheffield, S10
10 2RX, UK.

11 ²Sheffield Teaching Hospitals, Royal Hallamshire Hospital NHS Foundation Trust, Sheffield,
12 S10 2JF, UK.

13 ³School of Biological Sciences, University of Southampton, Southampton, SO17 1BJ, UK.

14 ⁴Swiss Light Source, Paul Scherrer Institut, Forschungsstrasse 111, 5232 Villigen-PSI,
15 Switzerland.

16 **Corresponding author: Dr Michelle Lawson**, Division of Clinical Medicine, School of
17 Medicine and Population Health, University of Sheffield, Beech Hill Road, Sheffield, S10 2RX.
18 m.a.lawson@sheffield.ac.uk

19

20

21

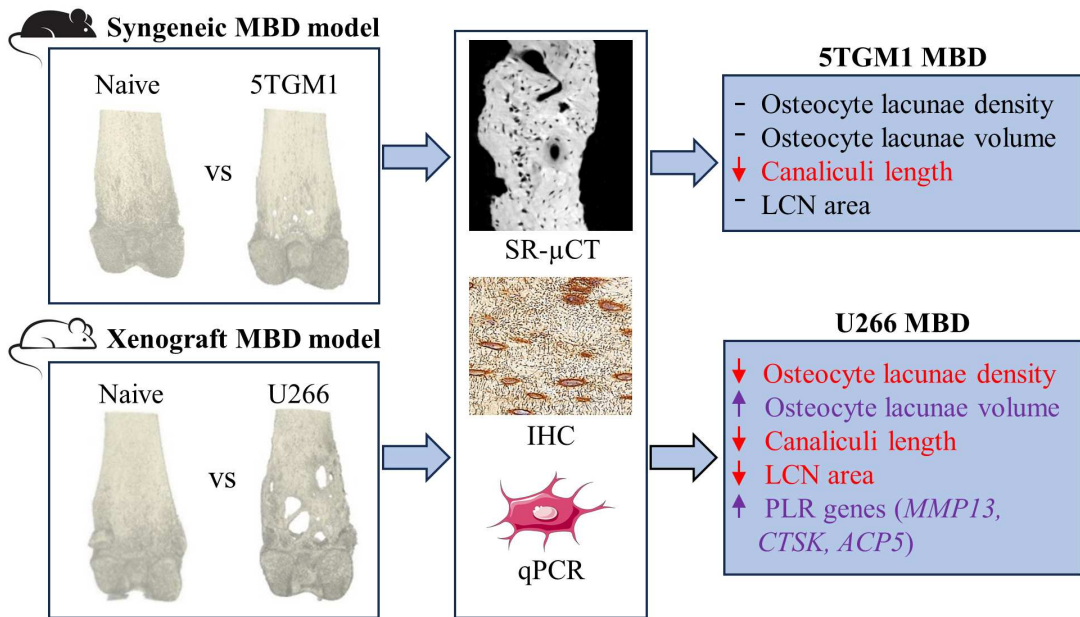
22

23 **Abstract**

24 Myeloma bone disease (MBD) affects approximately 90% of multiple myeloma patients but
25 current treatment options are suboptimal. Therefore, to successfully develop new therapies or
26 optimize current ones, we must improve our fundamental knowledge of how myeloma affects
27 bone microstructure and function. Here we have investigated the osteocyte lacuno-canalicular
28 network (LCN) in MBD, as bone porosity affects bone quality and resilience. We used the
29 syngeneic 5TGM1-C57BL-Kalwrij and the xenograft U266-NSG models at end stage and
30 compared them to healthy controls (naïve). Micro-computed tomography (μ CT) and
31 histomorphometry indicated the 5TGM1 and U266 models developed mild and extensive MBD
32 respectively, with the U266 model producing large osteolytic lesions. High-resolution
33 synchrotron micro-CT (SR- μ CT) revealed significant osteocyte lacunae changes in U266
34 bones but not 5TGM1, with a reduction in lacunae number and sphericity, and an increase in
35 lacunae volume compared to naïve. Canalicular length, visualized using histological Ploton
36 silver staining, appeared significantly shorter in 5TGM1 and U266 bones compared to naïve.
37 Canalicular area as a proportion of the bone was also decreased by 24.2% in the U266 model.
38 We observed significant upregulation of genes implicated in peri-lacunar remodeling (PLR),
39 but immunohistochemistry confirmed that the osteocyte-specific protein sclerostin, a known
40 driver of PLR, was unchanged between MBD and naïve bones. In summary, we have
41 demonstrated evidence of PLR and altered organization of the osteocyte LCN in MBD mouse
42 models. The next step would be to further understand the drivers and implications of PLR in
43 MBD, and whether treatments to manipulate PLR and the LCN may improve patient outcomes.

44

45 **Lay summary**



46 Multiple myeloma is a blood cancer that causes bone damage in approximately 90% of patients.
47 Currently treatment options for myeloma bone disease (MBD) are suboptimal, leaving patients
48 with chronic pain and increased fracture risk. Therefore, it is important that we improve our
49 fundamental knowledge of how myeloma causes bone damage. With the development of more
50 powerful imaging technologies, this allows us to visualize bone at the sub-micron level. Here
51 we assessed bones from two murine models of MBD (termed 5TGM1 and U266) and compared
52 them to bones from healthy control mice (naïve). Using high resolution imaging (SR- μ CT) we
53 found structural changes in the pores where the most abundant bone cells (osteocytes) reside,
54 and that the orientation of their signaling network (lacuno-canalicular network, LCN) is altered
55 in MBD compared to healthy bones. We also found differences in gene expression of key
56 molecules in osteocytes from bones with MBD compared to healthy bones and identified a
57 potential mechanism leading to these changes. The next step would be to use this knowledge
58 to determine how myeloma treatments can affect the osteocyte LCN, as this may allow
59 informed treatment decisions to be made, potentially reducing fracture risk and improving
60 outcomes for patients with MBD.

61

62 **Key words**

63 Myeloma, osteocytes, bone, lacuno-canalicular network, synchrotron, peri-lacunar remodeling

64

65 **Introduction**

66 Multiple myeloma is a blood cancer that develops in plasma cells in the bone marrow. Patients
67 often present with myeloma bone disease (MBD) caused by the uncoupling of bone remodeling,
68 resulting in osteolytic lesions and trabecular thinning.^[1] Current therapies, such as
69 bisphosphonates and denosumab (receptor activator of nuclear factor kappa- β ligand (RANKL)

70 inhibitor), target osteoclasts but often leave patients with high fracture risk, possibly due to
71 enhancement and propagation of micro-cracks over time.^[2] Therefore, to successfully develop
72 new therapies or optimize current ones, we must improve our fundamental knowledge of how
73 myeloma affects bone. Most research to date has focused on osteoblasts and osteoclasts, with
74 limited knowledge about osteocytes. Therefore, further research into the role of osteocytes and
75 their lacuno-canalicular network (LCN) in MBD is needed, both to fully understand their part
76 in MBD-induced bone fragility, and to further explore whether osteocytes could be targeted
77 therapeutically to treat MBD.

78

79 Osteocytes, comprising >90% of the total bone cell population,^[3] are derived from terminally
80 differentiated cells of the osteoblast lineage. They reside in lacunae embedded within the
81 mineralized bone matrix and form a dense, intricate dendritic network that allows them to
82 communicate with each other and other bone cells via the LCN.^[4] Osteocytes are key regulators
83 of bone remodeling, coordinating osteoblast and osteoclast proliferation and differentiation
84 through signaling pathways.^[5, 6] They produce sclerostin, a protein encoded by the *Sost* gene
85 that binds to LRP5/6 receptors and inhibits the Wnt pathway, leading to reduced bone
86 formation. Osteocytes also directly control bone homeostasis through a process called peri-
87 lacunar remodeling (PLR), whereby they resorb and replace the extracellular matrix,
88 comprising type I collagen, that directly surrounds them.^[7, 8] PLR has been demonstrated in
89 several mouse lactation studies,^[9, 10] but can occur in both male and female mice.^[11] Moreover,
90 it is initiated in conditions such as osteomalacia^[12] and rickets.^[13] Interestingly, sclerostin and
91 TGF β are known drivers of PLR,^[8, 14] both of which are known to be regulatory factors in
92 myeloma.

93 Studies have shown that patients with MBD have proportionally fewer viable osteocytes than
94 healthy controls.^[15] In preclinical MBD models, Ziouti *et al.*^[16] have observed enlarged
95 osteocyte lacunae and disorganization in the osteocyte LCN but these changes were not
96 quantified. There is mixed data regarding sclerostin expression in MBD. Giuliani *et al.*^[15]
97 found that sclerostin expression by osteocytes in myeloma patients was not significantly
98 different than that in healthy patients; in contrast, Terpos *et al.*^[17] reported that patients with
99 symptomatic myeloma had elevated circulating sclerostin compared to healthy patients or those
100 with monoclonal gammopathy of undetermined significance. These differences in sclerostin
101 may be explained by Delgado-Calle *et al.* who observed that myeloma cells increase osteocyte
102 apoptosis, both *in vitro* and *in vivo*, and that myeloma cells upregulate *Sost* (sclerostin gene)
103 mRNA levels in osteocytes *in vitro*.^[18] Contrastingly, McDonald *et al.* found minimal
104 difference in *Sost* expression in osteocytes from MBD mice at disease end stage, and no
105 difference in the number of sclerostin-positive osteocytes.^[19] Sclerostin expression may,
106 therefore, be dependent on the stage of MBD, limiting efficacy of anti-sclerostin therapies in
107 some patients. However, in preclinical models of MBD, sclerostin inhibition has shown great
108 promise,^[19] but as yet therapies such as romosozumab have not been used clinically in myeloma
109 patients, only in osteoporosis.^[20, 21]

110 Osteocytes play a clear role in bone homeostasis, yet much is unknown about how the osteocyte
111 LCN is implicated in MBD pathogenesis. Here, we hypothesized that MBD leads to increased
112 osteocyte apoptosis, resulting in a reduced and disorganized LCN that we can correlate to
113 sclerostin expression. To test this we used two mouse models, one with mild MBD (5TGM1)
114 and one with extensive MBD (U266), and then compared their bones to those from healthy
115 control (naïve, non-tumor controls) mice. Using Ploton silver staining and high-resolution
116 synchrotron micro-CT (SR- μ CT), we determined that osteocyte canaliculi appeared shorter in
117 both models, and in the highly osteolytic U266 bones there were fewer osteocyte lacunae.

118 However, these remaining lacunae were enlarged and the LCN appeared to have an altered
119 organization with reduced area coverage. Isolation of osteocyte-enriched RNA from marrow-
120 flushed U266 whole bones showed key PLR-related genes were upregulated, implying that
121 PLR may be driving the changes seen in the osteocyte lacunae and the LCN.

122 **Material and Methods**

123 *Ethical approval*

124 All animal experiments were approved by the University of Sheffield Animal Ethics
125 Committee and the UK Home Office (PPL PP3267943) in strict compliance with the Animal
126 (Scientific Procedures) Act 1986.

127 *Cell lines*

128 5TGM1-GFP and U266-GFP-Luc cells were maintained in RPMI 1640 medium with 10% fetal
129 bovine serum and 50 units/ml penicillin/100µg/ml streptomycin in an atmosphere of 5% CO₂
130 at 37°C. Cells were confirmed as negative for mycoplasma in the week preceding inoculation.

131 *In vivo studies*

132 5TGM1 model (syngeneic): 6-8 week-old male C57BL/KaLwRijHsd (BKAL) mice (Charles
133 River Laboratories, UK) were injected intravenously (i.v.) with 2x10⁶ 5TGM1-eGFP cells
134 (5TGM1 tumor group, n=8) or PBS (BKAL, naïve control group, n=5). All mice were
135 sacrificed at 3 weeks post-tumor cell injection.

136 U266 model (xenograft): 9-10 week-old female NOD *scid* gamma (NOD.Cg-
137 *Prkdc^{scid}Il2rg^{tm1Wjl}/SzJ*, NSG) mice were injected i.v. with 10⁶ U266-GFP-luc cells (U266
138 tumor group, n=8) or PBS (NSG, naïve control group, n=8). All mice were sacrificed at 10
139 weeks post-tumor cell injection. The U266 model and naïve mice (n=8 or 3/group, respectively)
140 were also used for quantitative real-time PCR (qPCR) of primary osteocytes.

141 All mice were randomized by weight and group-housed in individual cages with a 12-hour
142 light/dark cycle and had free access to food and water. Experimental mouse group numbers
143 were calculated using power calculations based on previously published data.^[22] All analyses
144 were performed blinded.

145 *Micro-computed tomography (μCT) and high-resolution synchrotron micro-CT imaging (SR-*
146 *μCT)*

147 Femora and tibiae were fixed in 10% formalin for 48 hours and then stored in 70% ethanol.
148 For *ex vivo* μCT, right femora were scanned on a Skyscan 1272 (Bruker, Switzerland) at 50kV
149 and 200μA at 4.3μm pixel resolution for a 180° scan with 0.7° rotation. A 1mm region of
150 interest 0.4μm from the growth plate was determined, and trabecular bone as a percentage of
151 bone volume (BV/TV), trabecular thickness (Tb. Th) trabecular number (Tb. N), trabecular
152 separation (Tb. Sp), cortical volume (Ct. V) and cortical thickness (Ct. Th) were assessed in
153 this region.as previously described.^[23] Bone lesion area as a proportion of total bone surface
154 area (%) was assessed using Osteolytica software as previously detailed.^[24]

155 Swiss Light Source (TOMCAT beamline, Paul Scherrer Institut, Switzerland, Proposal ID
156 20220399): Right 5TGM1 tibiae at the tibiofibular joint ^[25, 26] and right U266 femora at the
157 metaphysis were scanned using SR-μCT in absorption and inline phase-contrast imaging mode
158 with 0.65μm pixel size to visualize both bone and osteocytes within lacunae.^[27, 28] For each
159 scan, 3000 projection images were captured over a 360° rotation with a fixed energy of 21keV
160 and an exposure time of 120ms, at a sample-to-detector propagation distance of 40mm.

161 Diamond Light Source (I13-2 beamline, Didcot, UK, Proposal MG31801): Right 5TGM1
162 femora were scanned at the metaphysis using SR-μCT with 1.625μm pixel size. For each scan,
163 2000 projections were captured over a 360° rotation with a beam energy of 20keV, a ring
164 current of 300mA and an exposure time of 130ms.

165 *SR- μ CT image processing and analysis*

166 SR- μ CT datasets were processed, analyzed and imaged using the software Dragonfly (v. 2022
167 for Windows, Object Research Systems (ORS) Inc, Montreal, Canada).

168 To analyze the osteocyte lacunae, a region of interest (ROI) was selected for both the femoral
169 metaphysis and the tibiofibular joint. For the femoral metaphysis, this was a 0.5mm section
170 (769 slices) 0.1mm distally from the last visible remaining portion of the growth plate. For the
171 tibiofibular joint, this was a 0.5mm section (769 slices) 0.1mm distally from where the fibula
172 connected to the tibia. Femoral ROIs also went through the additional step of having their
173 trabecular bone removed from the dataset, leaving only the cortex.

174 For both femoral metaphysis and tibiofibular joint ROI datasets, firstly the cortex was
175 segmented from the background by global thresholding so that a binary image remained, where
176 cortex was white and background was black. A sweep was also performed so that only the
177 largest object remained, removing any unwanted artefacts. Next, a mask of the bone was
178 created, with all pores (not open to the outside) filled in. This was to serve as the base, so that
179 when the original, porous, bone was subtracted from it only the lacunae would remain. Pores
180 were then filtered by volume as reported by Hemmatian *et al.*^[29] with those of a volume less
181 than $2000\mu\text{m}^3$ classed as osteocyte lacunae. Those with a volume greater than $2000\mu\text{m}^3$ were
182 classed as intracortical canals and excluded. Pores with a volume less than $25\mu\text{m}^3$ were
183 assumed to be noise and were similarly excluded. Osteocyte lacunae were quantified for the
184 following parameters: density (number per mm^3 of cortical bone), proportion (% of cortical
185 bone), mean volume (μm^3) and sphericity (relative index, with 1 equaling a perfect sphere).

186 *Histomorphometry and immunohistochemistry*

187 Left tibiae were decalcified, wax embedded, then 3 μ m sections cut and stained for tartrate-
188 resistant acid phosphatase (TRAP) and hematoxylin as previously described.^[30] Quantification
189 of tumor burden, osteoclasts and osteoblasts were assessed as previously described.^[31]

190 For staining of the osteocyte lacuno-canalicular network, 3 μ m paraffin-embedded sections
191 were dewaxed and exposed to Ploton silver staining.^[32] Sections were stained with 50% silver
192 nitrate solution, and silver staining then developed in a 5% sodium thiosulphate solution.
193 Sections were also counterstained with hematoxylin for visualization of osteocyte nuclei.

194 The LCN was analyzed using Osteomeasure (Osteometrics, Decatur, GA, USA), Fiji (v. 1.543t,
195 National Institutes of Health, USA)^[33] and Dragonfly. For quantification of LCN coverage a
196 3-field 1.5mm region, 1.5mm from the growth plate, was assessed and microscope field images
197 taken every 0.5mm. Fiji was used to assess LCN area as a proportion of total bone area.
198 Microscope field images were loaded and for each a ROI encapsulating the entirety of the bone
199 area was drawn and any osteocytes and cement lines removed, so that only bone area and LCN
200 remained. The image was then binarized with the LCN becoming white and the bone surface
201 becoming black. LCN area as a proportion of total bone area was then calculated for each of
202 the 3 fields, before the mean was calculated. For quantification of osteocyte canalicular length,
203 canaliculi arising from each osteocyte lacuna and extending as a single, unbranched projection
204 were traced using Osteomeasure. The mean length was determined by loading microscope field
205 images and measuring all canaliculi from 3 osteocytes per field for a total of 9 osteocytes,
206 before an average canaliculi length was calculated, as previously carried out by Dole *et al.*^[8]

207 For 2-D analysis of LCN orientation, microscope field images were loaded into Dragonfly and
208 aligned so that osteocyte lacunae lay as straight to the horizontal plane as possible, with
209 canaliculi thus perpendicular to them in the vertical plane. The image was segmented, so that
210 the LCN became white and the surrounding bone became black. 2D orientation analysis was
211 then performed, with the angle of major axis of each canaliculus measured from the vertical in

212 degrees. Proportion of canaliculi falling between -20 degrees to 20 degrees around the vertical
213 out of all canaliculi was then assessed.

214 For sclerostin assessment, decalcified 3µm paraffin-embedded tibial sections were dewaxed
215 and treated with pepsin for antigen retrieval and 3% H₂O₂ for blocking of endogenous
216 peroxidase activity, followed by 10% casein for non-specific protein block. Sections were
217 incubated with primary sclerostin antibody (1:500, R&D, AF1589) followed by incubation
218 with a secondary biotinylated antibody (horse anti-goat IgG biotin, Vector BA – 100, 1:200).
219 Sections were then treated with an avidin-conjugated peroxidase (VectaStain Elite ABC-HROP
220 Kit, Vector Laboratories) and DAB (Vector, ImmPACT DAB, SK-4105). Sclerostin protein
221 was stained in brown and sections were counterstained with hematoxylin. Slides were scanned
222 on a NanoZoomer XR slide scanner (Hamamatsu, Shizuoka, Japan) at 40x, and sclerostin
223 coverage and number of sclerostin-positive osteocytes^[34] was quantified using QuPath (v.
224 0.4.3). A 1.5mm region, 250µm from the growth plate, was assessed.

225 *Quantitative real-time PCR (qPCR)*

226 Prior to sacrifice, presence of tumor and MBD were confirmed in U266 mice as previously
227 described.^[22] Right femora (after removal of soft tissue, distal and proximal ends, and marrow)
228 were snap frozen in liquid nitrogen and then homogenized (Precellys Evolution, Bertin
229 Instruments, France) in tri reagent (guanidinium thiocyanate).^[8] RNA was extracted using
230 phenol-chloroform and quantified using a Nanodrop spectrophotometer. cDNA was
231 synthesized using a High-Capacity RNA-to-cDNA kit (ThermoFisher Scientific) and qPCR
232 was performed on a QuantStudio 7 with Design and Analysis 2.6.0 software (Applied
233 Biosystems, CA, USA) with TaqMan primers used for quantification of *Dmp1* (*dentin matrix*
234 *acidic phosphoprotein 1*), *Sost*, *MMP13* (*matrix metalloproteinase-13*), *Ctsk* (*cathepsin K*),

235 *Acp5* (acid phosphatase 5, TRAP) and *MMP2* (matrix metalloproteinase-2) genes relative to
236 *Gapdh*.^[36]

237 *Statistical analysis*

238 All data are presented as mean \pm SD. Statistical analysis was performed using GraphPad Prism
239 9 (GraphPad Software, Inc., La Jolla, CA, USA) using unpaired two-tailed Student's t test.

240 **Results**

241 *Mice with 5TGM1 or U266 tumors exhibit myeloma bone disease*

242 To first verify that the 5TGM1 and U266 models (Fig 1A-B) successfully resulted in MBD we
243 assessed the bones for the presence of tumor cells, as well as changes in osteoblasts and
244 osteoclasts (Fig 1C-M). Tumor burden was high in both 5TGM1 and U266 (Fig 1C-F, K), and
245 both myeloma models exhibited decreased osteoblast surface coverage and osteoblast number
246 (Fig 1G-J, L, Supplemental Fig 1A). Osteoclast surface coverage and number remained
247 unchanged in the 5TGM1 model but rose significantly in the U266-bearing mice (Fig 1G-J, M,
248 Supplemental Figure 1B). Both myeloma models developed osteolytic lesions in the proximal
249 femur, although these were far more extensive (5-fold higher) in the U266 model (Fig 1N-Q,
250 T). Neither model exhibited lesions in the tibiofibular joint region (Fig 1R-S). For cortical bone,
251 5TGM1-bearing mice showed no significant change in either cortical volume or cortical
252 thickness compared to naïve, whereas U266-bearing mice exhibited a decreased cortical
253 volume whilst cortical thickness remained unchanged when compared to naïve (Fig 1U-V). For
254 trabecular bone architecture, 5TGM1-bearing mice showed no significant change in trabecular
255 bone volume, but U266-bearing mice exhibited a lower trabecular bone volume (Fig 1W) than
256 naïve controls. Trabecular thickness, trabecular number and trabecular separation were
257 unchanged between disease and naïve in both models (Supplemental Fig 1C-E).

258 *Osteocyte lacunae are enlarged and more ellipsoidal in U266 mice*

259 To determine whether the presence of MBD induced changes in osteocyte lacunae, we
260 examined the femoral metaphysis and tibiofibular joint by high-resolution SR- μ CT scanning
261 (Supplemental Fig 1F-J). At the femoral metaphysis, osteocyte lacunar density was unaffected
262 in 5TGM1 mice compared to naïve, but in U266 mice it was significantly decreased (Fig 2A).
263 Lacunar volume as a proportion of total bone volume was similarly unaffected in 5TGM1
264 compared to naïve, but significantly increased in U266 (Fig 2B). This increase in proportion
265 was driven by a significant doubling in average lacunar volume for U266 compared to naïve,
266 while average lacunar volume remained unchanged for 5TGM1 (Fig 2C, E-H). Lacunar
267 sphericity was also significantly altered in the U266 model with less spherical lacunae
268 compared to naïve, whilst there was no change in sphericity in 5TGM1 (Fig 2D). We also
269 examined the tibiofibular joint region in the 5TGM1 model compared to naïve (Fig 1R-S,
270 Supplementary Fig 1G); this region typically does not develop MBD, and we wanted to test
271 whether the changes in osteocytes found at the femoral metaphysis were systemic or localized.
272 No changes in osteocyte lacunar density, proportion, volume or sphericity were observed in
273 this region (Supplemental Fig 1K-P).

274 To confirm the enlarged lacunae in U266 bones still housed osteocytes and were not simply
275 empty pits, the lacunae were examined in SR- μ CT scans taken using phase-contrasting
276 techniques, which allows the visualization of both high-contrast objects (bone) and low-
277 contrast objects (osteocytes). Solid structures were clearly identifiable within the lacunae,
278 which we believe to be osteocytes. (Fig 2I-L).

279 *5TGM1 and U266 mice have osteocyte canaliculi of a shorter appearance compared to naïve*
280 *mice*

281 Osteocytes function as part of a complex dendritic network that allows them to communicate
282 with each other. We assessed if MBD altered the coverage and structure of the LCN. We treated

283 tibial sections with Ploton silver staining and examined a region at the tibial metaphysis.
284 Average apparent canaliculi length was significantly shorter in both 5TGM1 (30.4%) and U266
285 (29.1%) tibiae compared to naïve tibiae (Fig 3A, C-F). LCN area as a proportion of the bone
286 was also 24.2% lower in U266 tibiae compared to naïve, whilst 5TGM1 tibiae were unaffected
287 (Fig 3B, C-F). To determine whether LCN orientation was altered, the number of canaliculi
288 lying perpendicular to the osteocytes was measured as a proportion of all canaliculi (Fig 3G).
289 U266 tibiae exhibited fewer perpendicular canaliculi compared to naïve, indicating altered
290 LCN organization, whilst 5TGM1 LCN organization was unaffected (Fig 3H-L).

291 *Osteocytes from U266 femora have elevated expression of peri-lacunar remodeling genes*

292 Osteocytes are known to contribute to bone homeostasis by PLR, a process whereby bone
293 surrounding osteocytes is resorbed and deposited. Therefore, we investigated whether the
294 increased lacunar size was associated with PLR. We isolated primary femoral osteocytes from
295 the U266 and naïve (NSG) mice and performed qPCR (Fig 4A-C) for a panel of genes: *Dmp1*
296 and *Sost*, which are osteocyte-specific; and *MMP13*, *Ctsk*, *Acp5* and *MMP2*, which are all
297 genes known to be involved in PLR.^[14, 37-39] It should be noted that the widely used primary
298 osteocyte isolation technique^[8, 40, 41] does not exclude the possibility that other bone cells may
299 be present in the population, such as osteoclasts. However, *Dmp1* and *Sost* were highly
300 expressed in all samples, confirming a high purity of osteocytes in the population.^[40] *Dmp1*
301 showed a 0.49-fold change in U266 compared to naïve. For the PLR genes, *MMP13* showed a
302 4.9-fold increase; *Ctsk* a 3.2-fold increase and *Acp5* a 7.7-fold increase compared to naïve.
303 *MMP2*, although not significant, showed a trend for a 1.74-fold increase (p=0.065). Despite
304 the upregulation of PLR-specific genes, there was no significant change in *Sost* expression in
305 U266 mice compared to naïve. We did not perform qPCR analysis on the primary osteocytes
306 of 5TGM1 mice owing to their unchanged osteocyte lacunar morphology. To further examine
307 the upregulation of *Acp5* we examined histological sections of U266 bone after staining for

308 TRAP and found numerous incidences of visible TRAP staining around the nuclei of osteocytes
309 (Supplemental Fig 1Q-R). This helps confirm that the osteocytes are performing osteocytic
310 osteolysis and rules out the possibility that the larger osteocyte lacunae are due to newly formed
311 osteocytes, which typically present with larger lacunae. However, it was impossible to quantify
312 the TRAP staining around the osteocytes, owing to the TRAP staining being too faint as to be
313 confidently identified in many areas.

314 *Increased osteocyte activity is not associated with increased sclerostin production*

315 Since sclerostin is known to stimulate PLR,^[14] we next determined whether sclerostin protein
316 levels were increased in U266 bones, though based on the expression data we predicted no
317 significant differences would be seen between disease and naïve bones. Tibial metaphysis
318 sections were stained for sclerostin by IHC (Fig 4D-G) and sclerostin area as a proportion of
319 total bone area was found to be unchanged in disease tibiae (5TGM1 and U266) compared to
320 respective naïves (Fig 4H). Osteocytes were also tagged as to whether they were positive or
321 negative for sclerostin, and the proportion of sclerostin-positive osteocytes was found to be
322 unaltered between disease and naïve tibiae (Fig 4I).

323

324 **Discussion**

325 Bone disease affects over 90% of myeloma patients, exposing them to chronic pain and high
326 risk of fracture. Current treatments for MBD are limited as they do not repair damaged bones,
327 indicating an unmet clinical need. To improve the treatment of MBD our fundamental
328 knowledge of MBD, particularly the role of osteocytes, needs to improve. Here we set out to
329 understand more about the role of osteocytes and their LCN in MBD by comparing healthy
330 bones to myeloma-bearing bones.

331 Initially we determined the extent of MBD in two different mouse models and found that both
332 models developed high levels of tumor burden but had differing levels of MBD: mild MBD in
333 5TGM1 and extensive MBD in U266. SR- μ CT showed that osteocyte lacunae proximal to
334 extensive MBD in U266 mice were greatly enlarged and more ellipsoid in comparison to naïve
335 bones. This was not seen in 5TGM1. One reason for the discrepancy between models could be
336 the extent of the osteolytic disease; however, Hemmatian *et al.*^[42] reported enlarged osteocyte
337 lacunae in breast and prostate cancer models that both displayed extensive osteolytic disease,
338 but the magnitude of the size change was much smaller than we have found in myeloma.
339 Furthermore, they found the larger lacunae were proximal to osteosclerotic regions rather than
340 osteolytic regions. Another reason could be the timespan of the models used: U266 is a 9-week
341 model, whereas 5TGM1 and the breast and prostate models used by Hemmatian *et al.* are
342 shorter 3-week models, suggesting the osteocyte lacunae require time to become fully enlarged.
343 The discrepancy between the 5TGM1 and U266 model could be further tested by using the
344 JN3 model, which is a very aggressive 3-week human xenograft model of myeloma that results
345 in very severe MBD. Examining the osteocytes of JN3 mice would help to confirm whether it
346 is severity of disease or length of disease course that are driving the changes. Finally, it cannot
347 be discounted that 5TGM1 mice have a functional immune system, whereas U266 mice are
348 immunocompromised, and that the presence of an immune system may be why fewer osteocyte
349 and LCN changes are seen in the 5TGM1. This could be tested by examining osteocytes in a
350 more long-course syngeneic model of myeloma such as the 5T2 model;^[43] however, access to
351 this mouse model is very limited at present.

352 We found that substantial MBD decreased osteocyte lacunae density by approximately 20%,
353 in keeping with what has been demonstrated clinically in patients.^[15] Vashishth *et al.* have
354 shown that decreased osteocyte density is correlated to an increased accumulation of
355 microcracks, indicating that a dense osteocyte network is linked to better bone quality.^[44] We

356 then quantified, for the first time to our knowledge, that MBD leads to an apparent decreased
357 osteocyte canalicular length and overall LCN coverage, and that extensive MBD causes the
358 LCN to be organized differently; similar observational findings were described by Ziouti *et*
359 *al.*^[16] The mechanisms behind this apparent canalicular shortening and disorganization are
360 currently unknown, and more work is required to determine how it comes about. It should also
361 be reiterated that the canaliculi were only assessed in 2-D, and that 3-D analysis using a
362 technique such as fluorochromes and confocal microscopy would be beneficial to confirm the
363 shortened canaliculi. However, changes in the LCN such as reduced coverage and shortened
364 canaliculi can affect the mechano-sensing perception of osteocytes, diminishing their ability to
365 initiate appropriate bone remodeling in response to loading or microfracture.^[45] These findings
366 may have further reaching clinical implications, as Ding *et al.* demonstrated in their partial
367 osteocyte-ablation murine model that when osteocyte numbers were reduced, rapid
368 development of osteoporosis and signs of early ageing were observed.^[46]

369 Osteocytes are known to help maintain bone homeostasis through processes such as sclerostin
370 secretion and PLR. We found no changes either in *Sost* upregulation in osteocytes or localized
371 sclerostin production, concurring with the findings of McDonald *et al.*^[19] but contradicting
372 other reported findings. The role of sclerostin in myeloma is clearly complex, and these
373 contrasting conclusions may be due to sclerostin levels fluctuating depending on the severity
374 of MBD and the timepoint at which they are measured in the disease course. It is also true that
375 sclerostin is expressed by other cells within the bone marrow, such as hypertrophic
376 chondrocytes,^[47] and that MBD may further influence these expression pathways. However,
377 we did determine that PLR-specific genes were upregulated in osteocyte-enriched populations
378 from bones of extensive MBD-bearing mice. The resorption part-process of PLR (also known
379 as osteocytic osteolysis) involves osteocytes secreting matrix metalloproteinases and enzymes
380 such as cathepsin K and TRAP to dissolve the surrounding bone matrix, and the upregulation

381 of these related genes provides evidence that PLR is contributing to bone loss in myeloma. To
382 our knowledge, this is the first time that PLR has been proposed as a mechanism of MBD
383 pathophysiology. Interestingly, since sclerostin is known to be a promotor of PLR and its levels
384 in osteocytes were unaffected, other potential drivers of the observed increase in PLR are still
385 to be identified. Aberrant PLR is clearly detrimental to bone health, and this leads to the
386 question of whether PLR-specific genes could be targeted therapeutically in order to normalize
387 osteocyte function. This opens up future avenues of exploration into the cause and consequence
388 of PLR in myeloma.

389 In summary, we have identified that extensive MBD leads to a decrease in the osteocyte
390 population and an enlargement of osteocyte lacunae. The osteocyte LCN is compromised by
391 MBD, with decreased canalicular length, network area coverage and altered organization. PLR-
392 specific genes are upregulated in the osteocytes in MBD, and further work is needed to explore
393 the ramifications of PLR in myeloma.

394 **Data Availability Statement**

395 The authors confirm that the data supporting the findings of this study are available within the
396 article [and/or] its supplementary materials.

397 **Disclaimers**

398 The authors have no conflicts to report.

399 **Author Contributions**

400 **Holly Evans:** investigation; methodology; formal analysis; interpretation; writing – original
401 draft; review and editing. **Rebecca Andrews:** conceptualization; funding acquisition;
402 investigation; interpretation; writing – original draft; review and editing. **Fatma Ali Abedi:**
403 investigation; formal analysis; writing – review and editing. **Alexandria Sprules:** investigation;

404 formal analysis; writing – review and editing. **Jacob Trend:** methodology; investigation;
405 writing – review and editing. **Goran Lovric:** methodology; writing – review and editing.
406 **Alanna Green:** conceptualization; funding acquisition; writing – review and editing. **Andrew**
407 **Chantry:** funding acquisition; supervision; writing – review and editing. **Janet Brown:**
408 funding acquisition; supervision; writing – review and editing. **Claire Clarkin:** funding
409 acquisition; methodology; writing – review and editing. **Michelle Lawson:** conceptualization;
410 funding acquisition; supervision; interpretation; writing – original draft; review and editing.

411 **Acknowledgements**

412 This work was supported by a Sheffield Hospitals Charity project grant (222323 to RA(PI),
413 HE and ML). Original *in vivo* experiment costs were supported by a Sheffield Hospitals Charity
414 project grant (163969 to RA(PI), AC and ML) and Weston Park Cancer Charity Clinical
415 Research Fellowship (RA (the named clinical fellow), AC, JB). The travel to the SR- μ CT
416 facility was funded by a European Association of Cancer Research (EACR) travel award
417 (awarded to RA) and the University of Sheffield travel award (ML). We acknowledge the Paul
418 Scherrer Institut, Villigen, Switzerland for provision of synchrotron radiation beamtime at the
419 TOMCAT beamline X02DA of the SLS (Proposal ID 20220399; HE, RA, AG, ML). The
420 Diamond Light Source is acknowledged for providing beamtime on I13-2 beamline under the
421 experiment number MG31801 (Proposal MG31801; JT), and we thank Dr
422 Shashidhara Marathe for his technical guidance. We also thank Dr Georgia Stewart, Ms Orla
423 Gallagher and Mr Aytac Gul for their technical expertise.

424 **References**

- 425 [1] Ring ES, Lawson MA, Snowden JA, et al. New agents in the Treatment of Myeloma
426 Bone Disease[J]. *Calcif Tissue Int* 2018,102(2):196-209.
427 [2] Rosenthal Y, Arami A, Kosashvili Y, et al. Atypical fractures of the femur related to
428 prolonged treatment with bisphosphonates for osteoporosis[J]. *Isr Med Assoc J*
429 2014,16(2):78-82.

430 [3] Dallas SL, Prideaux M, Bonewald LF. The osteocyte: an endocrine cell ... and more[J].
431 *Endocr Rev* 2013,34(5):658-90.

432 [4] Creecy A, Damrath JG, Wallace JM. Control of Bone Matrix Properties by Osteocytes[J].
433 *Front Endocrinol (Lausanne)* 2020,11:578477.

434 [5] Bonewald LF. The amazing osteocyte[J]. *J Bone Miner Res* 2011,26(2):229-38.

435 [6] Schaffler MB, Cheung WY, Majeska R, et al. Osteocytes: master orchestrators of bone[J].
436 *Calcif Tissue Int* 2014,94(1):5-24.

437 [7] Tsourdi E, Jahn K, Rauner M, et al. Physiological and pathological osteocytic
438 osteolysis[J]. *J Musculoskelet Neuronal Interact* 2018,18(3):292-303.

439 [8] Dole NS, Mazur CM, Acevedo C, et al. Osteocyte-Intrinsic TGF-beta Signaling Regulates
440 Bone Quality through Perilacunar/Canalicular Remodeling[J]. *Cell Rep* 2017,21(9):2585-
441 2596.

442 [9] Qing H, Ardeshirpour L, Pajevic PD, et al. Demonstration of osteocytic
443 perilacunar/canalicular remodeling in mice during lactation[J]. *J Bone Miner Res*
444 2012,27(5):1018-29.

445 [10] Li Y, de Bakker CMJ, Lai X, et al. Maternal bone adaptation to mechanical loading
446 during pregnancy, lactation, and post-weaning recovery[J]. *Bone* 2021,151:116031.

447 [11] Asagiri M, Takayanagi H. The molecular understanding of osteoclast differentiation[J].
448 *Bone* 2007,40(2):251-64.

449 [12] Rolvien T, Krause M, Jeschke A, et al. Vitamin D regulates osteocyte survival and
450 perilacunar remodeling in human and murine bone[J]. *Bone* 2017,103:78-87.

451 [13] Tokarz D, Martins JS, Petit ET, et al. Hormonal Regulation of Osteocyte Perilacunar and
452 Canalicular Remodeling in the Hyp Mouse Model of X-Linked Hypophosphatemia[J]. *J Bone*
453 *Miner Res* 2018,33(3):499-509.

454 [14] Kogawa M, Wijenayaka AR, Ormsby RT, et al. Sclerostin regulates release of bone
455 mineral by osteocytes by induction of carbonic anhydrase 2[J]. *J Bone Miner Res*
456 2013,28(12):2436-48.

457 [15] Giuliani N, Ferretti M, Bolzoni M, et al. Increased osteocyte death in multiple myeloma
458 patients: role in myeloma-induced osteoclast formation[J]. *Leukemia* 2012,26(6):1391-401.

459 [16] Ziouti F, Soares AP, Moreno-Jimenez I, et al. An Early Myeloma Bone Disease Model
460 in Skeletally Mature Mice as a Platform for Biomaterial Characterization of the Extracellular
461 Matrix[J]. *J Oncol* 2020,2020:3985315.

462 [17] Terpos E, Christoulas D, Katodritou E, et al. Elevated circulating sclerostin correlates
463 with advanced disease features and abnormal bone remodeling in symptomatic myeloma:
464 reduction post-bortezomib monotherapy[J]. *Int J Cancer* 2012,131(6):1466-71.

465 [18] Delgado-Calle J, Anderson J, Cregor MD, et al. Bidirectional Notch Signaling and
466 Osteocyte-Derived Factors in the Bone Marrow Microenvironment Promote Tumor Cell
467 Proliferation and Bone Destruction in Multiple Myeloma[J]. *Cancer Res* 2016,76(5):1089-
468 1100.

469 [19] McDonald MM, Reagan MR, Youlten SE, et al. Inhibiting the osteocyte-specific protein
470 sclerostin increases bone mass and fracture resistance in multiple myeloma[J]. *Blood*
471 2017,129(26):3452-3464.

472 [20] Cosman F, Crittenden DB, Adachi JD, et al. Romosozumab Treatment in
473 Postmenopausal Women with Osteoporosis[J]. *N Engl J Med* 2016,375(16):1532-1543.

474 [21] Lewiecki EM, Blicharski T, Goemaere S, et al. A Phase III Randomized Placebo-
475 Controlled Trial to Evaluate Efficacy and Safety of Romosozumab in Men With
476 Osteoporosis[J]. *J Clin Endocrinol Metab* 2018,103(9):3183-3193.

477 [22] Paton-Hough J, Tazzyman S, Evans H, et al. Preventing and Repairing Myeloma Bone
478 Disease by Combining Conventional Antiresorptive Treatment With a Bone Anabolic Agent
479 in Murine Models[J]. *J Bone Miner Res* 2019,34(5):783-796.

480 [23] Green AC, Lath D, Hudson K, et al. TGFbeta Inhibition Stimulates Collagen Maturation
481 to Enhance Bone Repair and Fracture Resistance in a Murine Myeloma Model[J]. *J Bone*
482 *Miner Res* 2019,34(12):2311-2326.

483 [24] Evans HR, Karmakharm T, Lawson MA, et al. Osteolytica: An automated image
484 analysis software package that rapidly measures cancer-induced osteolytic lesions in in vivo
485 models with greater reproducibility compared to other commonly used methods[J]. *Bone*
486 2016,83:9-16.

487 [25] Nunez JA, Goring A, Javaheri B, et al. Regional diversity in the murine cortical vascular
488 network is revealed by synchrotron X-ray tomography and is amplified with age[J]. *Eur Cell*
489 *Mater* 2018,35:281-299.

490 [26] Nunez JA, Goring A, Hesse E, et al. Simultaneous visualisation of calcified bone
491 microstructure and intracortical vasculature using synchrotron X-ray phase contrast-enhanced
492 tomography[J]. *Sci Rep* 2017,7(1):13289.

493 [27] Paganin D, Mayo SC, Gureyev TE, et al. Simultaneous phase and amplitude extraction
494 from a single defocused image of a homogeneous object[J]. *J Microsc* 2002,206(Pt 1):33-40.

495 [28] Lovric G, Oberta P, Mohacsi I, et al. A robust tool for photon source geometry
496 measurements using the fractional Talbot effect[J]. *Opt Express* 2014,22(3):2745-60.

497 [29] Hemmatian H, Laurent MR, Ghazanfari S, et al. Accuracy and reproducibility of mouse
498 cortical bone microporosity as quantified by desktop microcomputed tomography[J]. *PLoS*
499 *One* 2017,12(8):e0182996.

500 [30] Lawson MA, Paton-Hough JM, Evans HR, et al. NOD/SCID-GAMMA mice are an
501 ideal strain to assess the efficacy of therapeutic agents used in the treatment of myeloma bone
502 disease[J]. *PLoS One* 2015,10(3):e0119546.

503 [31] Lath DL, Buckle CH, Evans HR, et al. ARQ-197, a small-molecule inhibitor of c-Met,
504 reduces tumour burden and prevents myeloma-induced bone disease in vivo[J]. *PLoS One*
505 2018,13(6):e0199517.

506 [32] Ploton D, Menager M, Jeannesson P, et al. Improvement in the staining and in the
507 visualization of the argyrophilic proteins of the nucleolar organizer region at the optical
508 level[J]. *Histochem J* 1986,18(1):5-14.

509 [33] Schindelin J, Arganda-Carreras I, Frise E, et al. Fiji: an open-source platform for
510 biological-image analysis[J]. *Nat Methods* 2012,9(7):676-82.

511 [34] Ikpegbu E, Basta L, Clements DN, et al. FGF-2 promotes osteocyte differentiation
512 through increased E11/podoplanin expression[J]. *J Cell Physiol* 2018,233(7):5334-5347.

513 [35] Bankhead P, Loughrey MB, Fernandez JA, et al. QuPath: Open source software for
514 digital pathology image analysis[J]. *Sci Rep* 2017,7(1):16878.

515 [36] Livak KJ, Schmittgen TD. Analysis of relative gene expression data using real-time
516 quantitative PCR and the 2(-Delta Delta C(T)) Method[J]. *Methods* 2001,25(4):402-8.

517 [37] Mazur CM, Woo JJ, Yee CS, et al. Osteocyte dysfunction promotes osteoarthritis
518 through MMP13-dependent suppression of subchondral bone homeostasis[J]. *Bone Res*
519 2019,7:34.

520 [38] Fowler TW, Acevedo C, Mazur CM, et al. Glucocorticoid suppression of osteocyte
521 perilacunar remodeling is associated with subchondral bone degeneration in osteonecrosis[J].
522 *Sci Rep* 2017,7:44618.

523 [39] Inoue K, Mikuni-Takagaki Y, Oikawa K, et al. A crucial role for matrix
524 metalloproteinase 2 in osteocytic canalicular formation and bone metabolism[J]. *J Biol Chem*
525 2006,281(44):33814-24.

526 [40] Youlten SE, Kemp JP, Logan JG, et al. Osteocyte transcriptome mapping identifies a
527 molecular landscape controlling skeletal homeostasis and susceptibility to skeletal disease[J].
528 *Nat Commun* 2021,12(1):2444.

529 [41] Dole NS, Yee CS, Schurman CA, et al. Assessment of Osteocytes: Techniques for
530 Studying Morphological and Molecular Changes Associated with Perilacunar/Canalicular
531 Remodeling of the Bone Matrix[J]. *Methods Mol Biol* 2021,2230:303-323.
532 [42] Hemmatian H, Conrad S, Furesi G, et al. Reorganization of the osteocyte lacuno-
533 canalicular network characteristics in tumor sites of an immunocompetent murine model of
534 osteotropic cancers[J]. *Bone* 2021,152:116074.
535 [43] Croese JW, Vas Nunes CM, Radl J, et al. The 5T2 mouse multiple myeloma model:
536 characterization of 5T2 cells within the bone marrow[J]. *Br J Cancer* 1987,56(5):555-60.
537 [44] Vashishth D, Verborgt O, Divine G, et al. Decline in osteocyte lacunar density in human
538 cortical bone is associated with accumulation of microcracks with age[J]. *Bone*
539 2000,26(4):375-80.
540 [45] Price C, Zhou X, Li W, et al. Real-time measurement of solute transport within the
541 lacunar-canalicular system of mechanically loaded bone: direct evidence for load-induced
542 fluid flow[J]. *J Bone Miner Res* 2011,26(2):277-85.
543 [46] Ding P, Gao C, Gao Y, et al. Osteocytes regulate senescence of bone and bone
544 marrow[J]. *Elife* 2022,11.
545 [47] Winkler DG, Sutherland MK, Geoghegan JC, et al. Osteocyte control of bone formation
546 via sclerostin, a novel BMP antagonist[J]. *EMBO J* 2003,22(23):6267-76.

547

548

549 **Figure legends**

550 **Figure 1. Extent of myeloma bone disease in 5TGM1 and U266 murine models.** Study
551 schematics of (A) 5TGM1 and (B) U266 models, BKAL and NSG mice were used as naïve
552 control groups respectively. Representative images of tibial hematoxylin-stained sections of
553 bone marrow from (C) naïve (BKAL) and (D) 5TGM1, and (E) naïve (NSG) and (F) U266.
554 Tibial TRAP-stained sections show endocortical bone surface of (G) naïve (BKAL) and (H)
555 5TGM1, and (I) naïve (NSG) and (J) U266, showing distribution of osteoblasts (red arrows)
556 and osteoclasts (blue arrows). Histomorphometric analysis of (K) tumor burden, (L) osteoblast
557 surface and (M) osteoclast surface. Representative images of bone lesions and trabecular
558 structure found in the distal femur of (N) naïve (BKAL) and (O) 5TGM1, and (P) naïve (NSG)
559 and (Q) U266; tibiofibular joint region of (R) naïve (BKAL) and (S) 5TGM1; and μ CT analysis
560 at the distal femur assessing (T) osteolytic lesion area, (U) cortical bone volume, (V) cortical
561 thickness and (W) trabecular bone volume. BM=bone marrow, T=tumor, EC=endocortical.

562 Data are presented as mean \pm SD. * p <0.05, ** p <0.01, *** p <0.001, **** p <0.0001 (unpaired
563 two-tailed Student's t-test).

564

565 **Figure 2. Osteocyte lacunae density is less in U266 mice with larger and more ellipsoidal**
566 **lacunae.** SR- μ CT analysis of the osteocyte lacunae in 5TGM1, U266 or respective naive mice
567 at the femoral metaphysis showing (A) osteocyte lacunae density, (B) osteocyte lacunae as a
568 proportion of the bone, (C) average osteocyte lacunar volume, and (D) average osteocyte
569 lacunar sphericity. Representative images of (E) naïve (BKAL), (F) 5TGM1, (G) naïve (NSG)
570 and (H) U266 femoral metaphysis regions assessed by SR- μ CT with individual osteocyte
571 lacunae false color-mapped by volume. Representative SR- μ CT images of (I) naïve (NSG) and
572 (J) U266 mice femoral cortical bone showing typical osteocyte lacunae. Phase-contrast
573 imaging of the same U226 bone using false-color mapping and (L) zoomed-in imaging showing
574 dark blue osteocytes sitting within the enlarged osteocyte lacunae (white arrows). BV=blood
575 vessel, OL=osteolytic lesion. All data shown as mean \pm SD. ** p <0.01, *** p <0.001,
576 **** p <0.0001 (unpaired two-tailed Student's t-test).

577

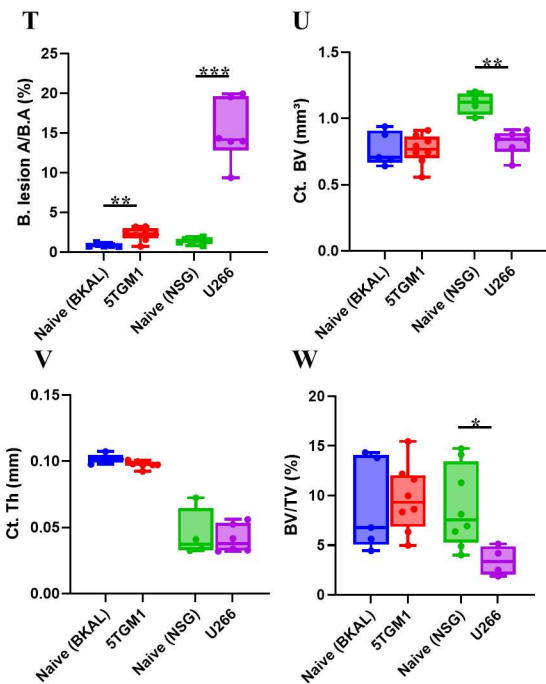
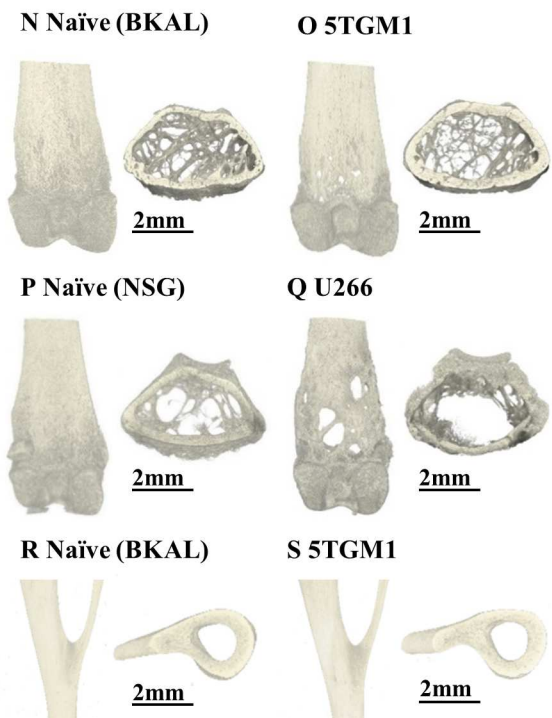
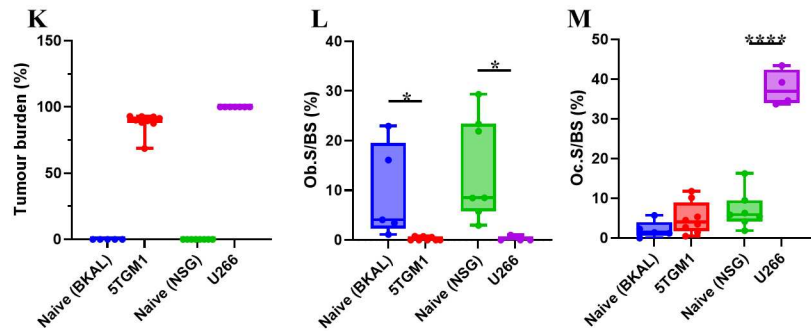
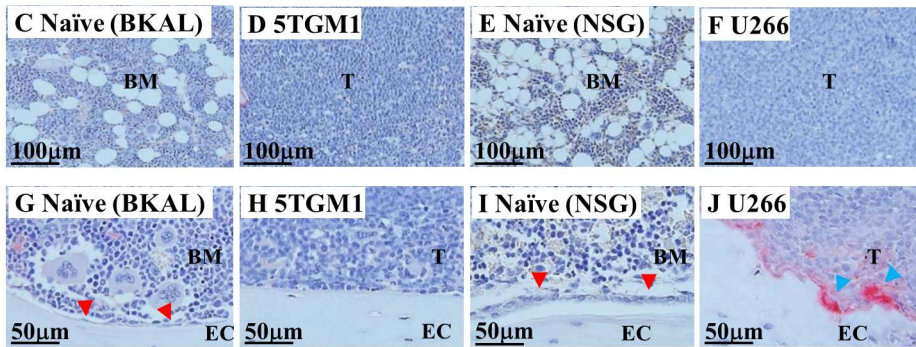
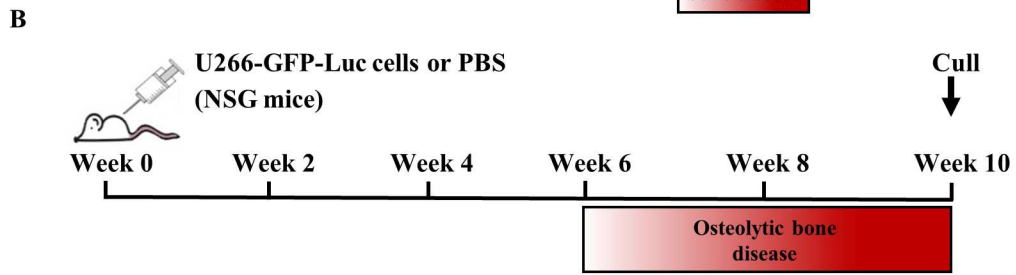
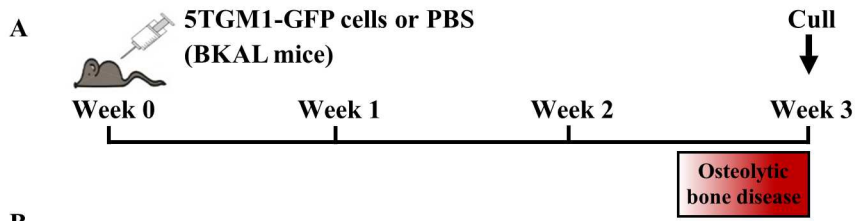
578 **Figure 3. Myeloma bone disease leads to apparent shortening of osteocyte canalicular**
579 **length and decreased LCN area coverage.** Analysis of the LCN showing (A) canalicular
580 length and (B) LCN area coverage. Representative Ploton silver nitrate-stained images of tibial
581 cortical bone of (C) naïve (BKAL), (D) 5TGM1, (E) naïve (NSG) and (F) U266, showing
582 osteocytes and the LCN. Analysis of LCN organization by (G) aligning osteocytes
583 perpendicular to bone lamellae (0°) and assessing degrees of alignment of canaliculi to 0° , and
584 (H) proportion of canaliculi aligned within 40° of 0° . Representative images of canalicular
585 orientation of (I) naïve (BKAL), (J) 5TGM1, (K) naïve (NSG) and (L) U266, with aligned

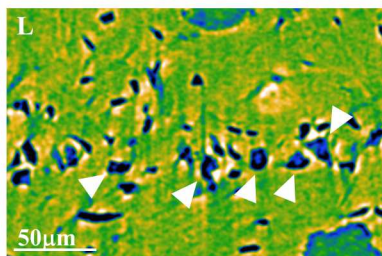
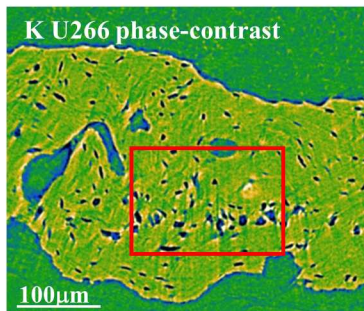
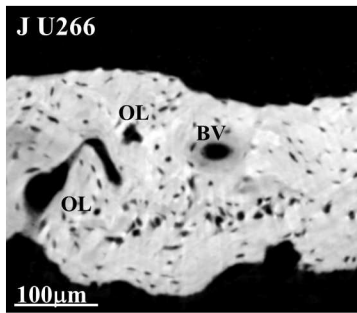
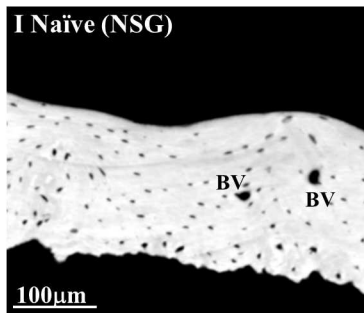
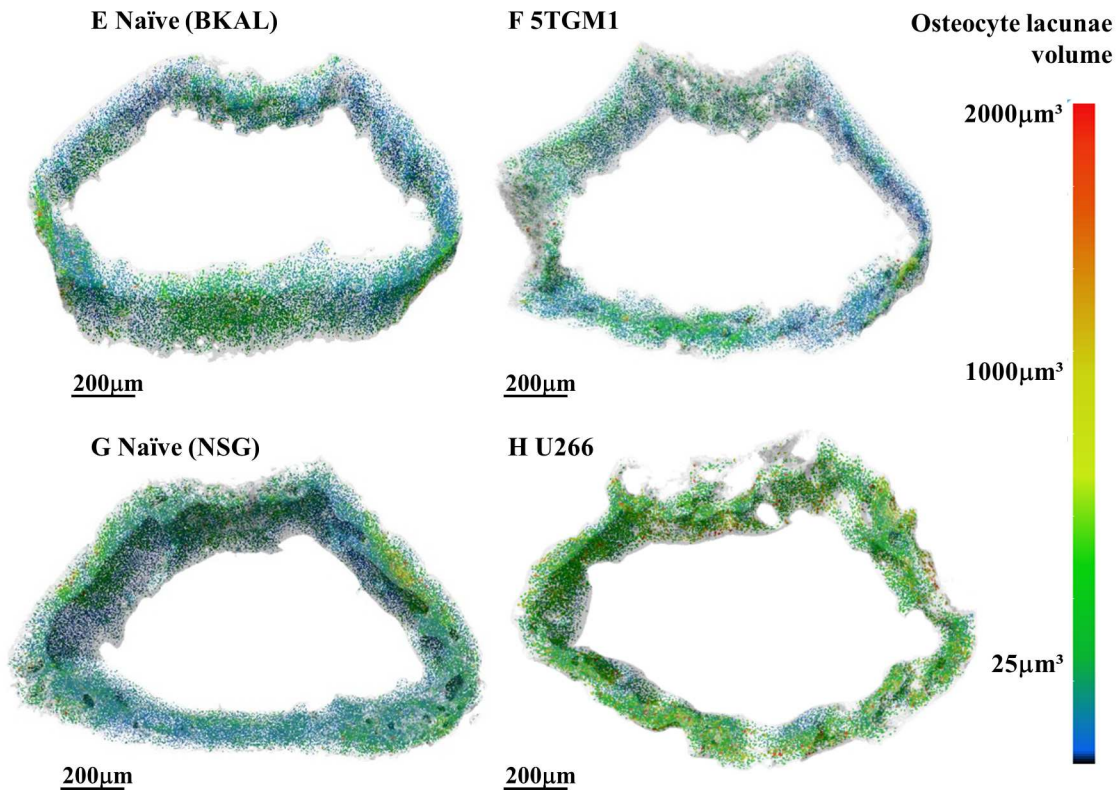
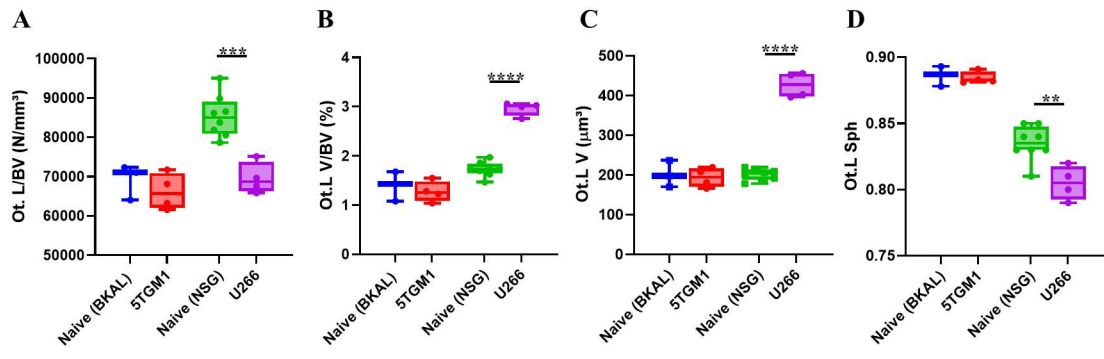
586 canaliculi in blue and unaligned canaliculi in red. All data shown as mean \pm SD. * $p < 0.05$,
587 ** $p < 0.01$, **** $p < 0.0001$ (unpaired two-tailed Student's t-test).

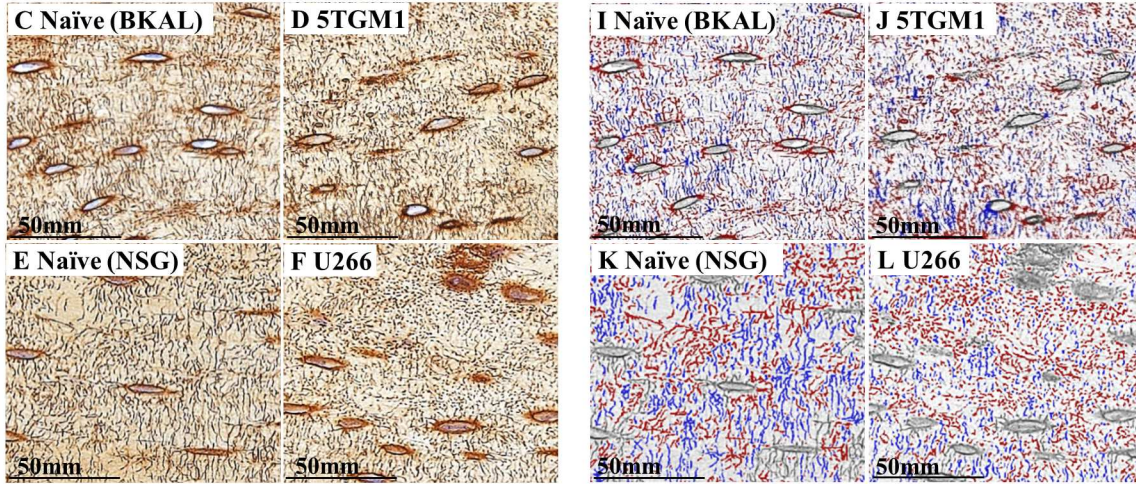
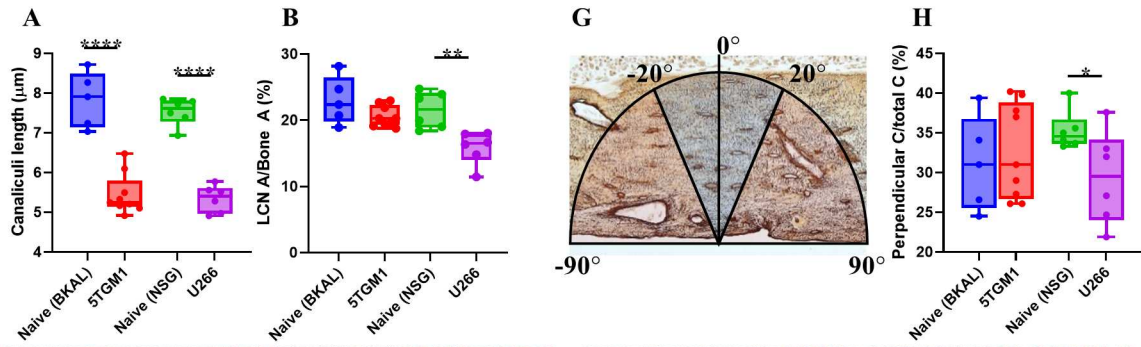
588

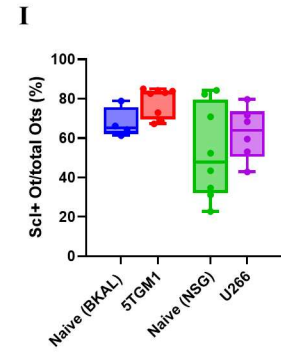
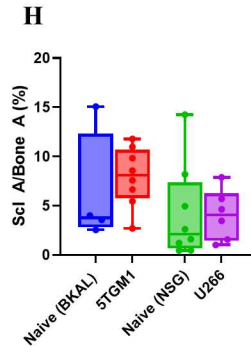
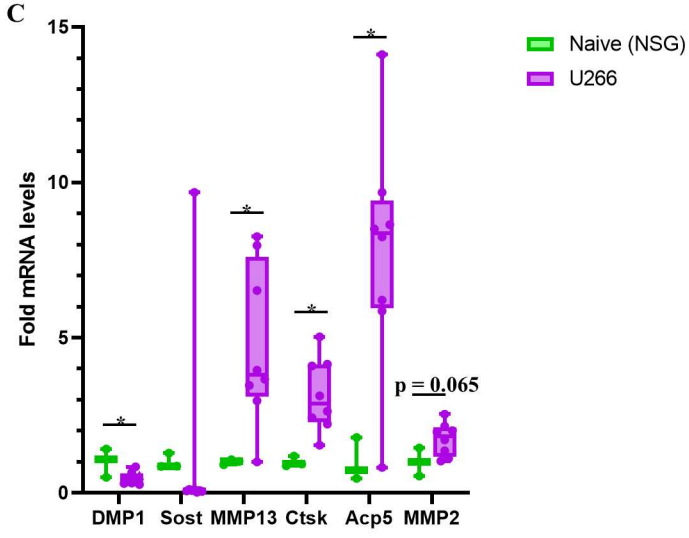
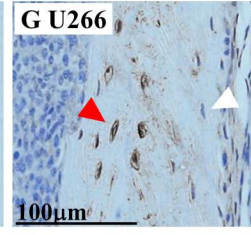
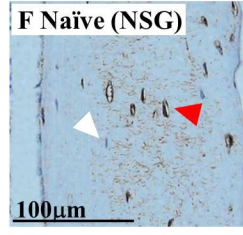
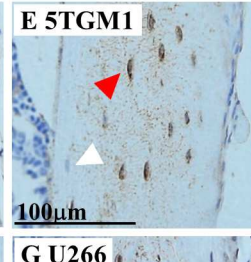
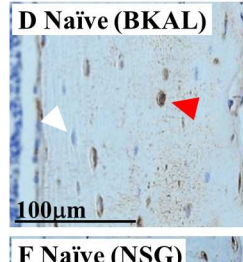
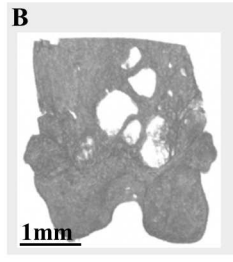
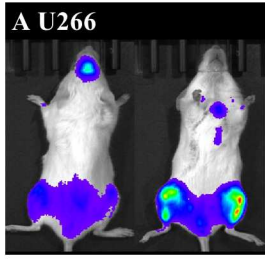
589 **Figure 4. Myeloma bone disease leads to up-regulation of PLR-specific genes but not *Sost*.**

590 Representative bioluminescent imaging of U266 tumor burden (A) and *in vivo* μ CT of the distal
591 femur (B) showing bone lesions. (C) qPCR analysis of osteocyte-specific genes *Dmp1* and *Sost*,
592 and PLR genes *MMP13*, *Ctsk*, *Acp5* and *MMP2* relative to *Gapdh* expression. Representative
593 images of sclerostin staining of tibial cortical bone of (D) naïve (BKAL), (E) 5TGM1, (F) naïve
594 (NSG) and (G) U266, with red arrows indicating sclerostin-positive osteocytes and white
595 arrows indicating sclerostin-negative osteocytes. Analysis of sclerostin IHC showing (H)
596 proportional sclerostin staining coverage and (I) proportion of sclerostin-positive osteocytes.
597 All data shown as mean \pm SD. * $p < 0.05$ (unpaired two-tailed Student's t-test).









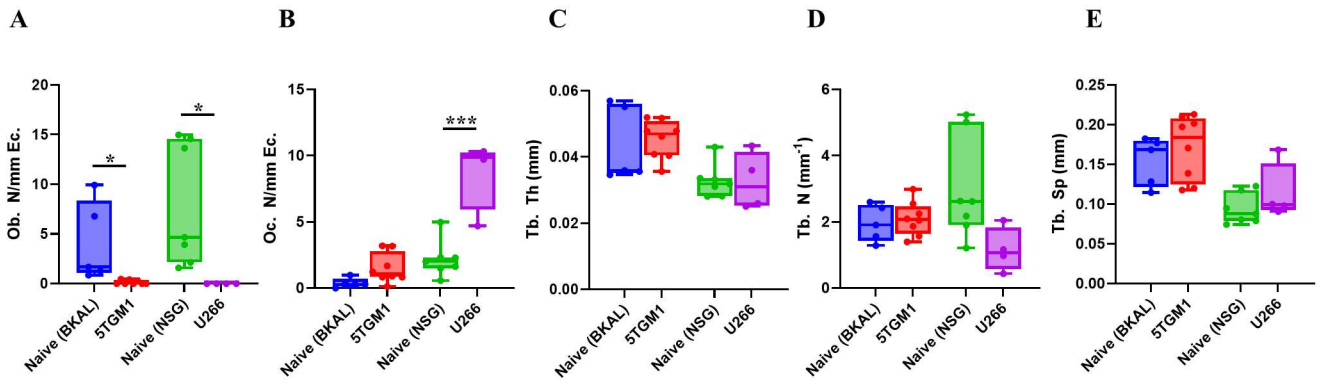
1 **Supplementary figure legends**

2

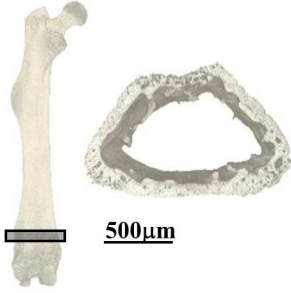
3 **Supplementary Figure 1. Osteocytes are unchanged at the TFJ in 5TGM1 mice.**

4 Histomorphometric analysis of (A) osteoblast number and (B) osteoclast number. μ CT analysis
5 at the distal femur assessing (C) trabecular thickness, (D) trabecular number and (E) trabecular
6 separation. Representative images of (F) the femoral metaphysis region scanned highlighted
7 by the black box and the resulting 500 μ m region imaged and analyzed at 0.65 μ m resolution
8 and (G) the tibiofibular joint region scanned highlighted by the black box and the resulting
9 500 μ m region imaged and analyzed at 0.65 μ m resolution. (H) Image of a femur to be scanned,
10 mounted on a metal chuck and glued in place. Representative image of (I) the femoral
11 metaphysis showing successfully isolated osteocyte lacunae in yellow and (J) a zoomed-in
12 region showing the successful exclusion of blood vessels (white arrows). SR- μ CT analysis of
13 the osteocyte lacunae in 5TGM1 at the tibiofibular joint showing (K) osteocyte lacunae density,
14 (L) osteocyte lacunae volume as proportion of the bone, (M) average osteocyte lacunar volume
15 and (N) average osteocyte lacunar sphericity. Representative images of (O) naïve (BKAL) and
16 (P) 5TGM1 tibiofibular joint regions with the individual osteocyte lacunae false color-mapped
17 by volume. Representative images of tibial TRAP-stained sections of endocortical bone of (Q)
18 naïve (NSG) and (R) U266, 1.5mm from the growth plate, showing osteocytes (red arrows)
19 and TRAP staining (pink). Osteoclasts are also highlighted (blue arrows). BM=bone marrow,
20 EC=endocortical. All data shown as mean \pm SD. * <0.05 , *** $p<0.001$ (unpaired two-tailed
21 Student's t-test).

22



F Femoral metaphysis



G Tibiofibular joint

